

Manipulating terahertz phonon-polariton in the ultrastrong coupling regime with bound states in the continuum

Jiaying Yang¹, Kai Wang^{1,2}, Liyu Zhang¹, Chen Zhang¹, Aoyu Fan³, Zijian He¹, Zhidi Li¹,
Xiaobo Han⁴, Furi Ling^{3*}, Peixiang Lu^{1,4*}*

¹Wuhan National Laboratory for Optoelectronics and School of Physics, Huazhong University of Science and Technology, Wuhan 430074, China

²School of Electronic and Information Engineering, Hubei University of Science and Technology, Xianning 437100, China

³School of Optics and Electronic Information, Huazhong University of Science and Technology Wuhan, Hubei 430074, P.R. China

⁴Hubei Key Laboratory of Optical Information and Pattern Recognition, Wuhan Institute of Technology, Wuhan 430205, China

*Corresponding authors:

kale_wong@hust.edu.cn (KW), lingfuri@mail.hust.edu.cn (FRL), lupeixiang@hust.edu.cn (PXL)

Abstract

The strong coupling between photons and phonons in polar materials gives rise to phonon-polaritons that encapsulate a wealth of physical information, offering crucial tools for the ultrafast terahertz sources and the topological engineering of terahertz light. However, it is still quite challenging to form and manipulate the terahertz phonon-polaritons under the ultrastrong coupling regime till now. In this work, we demonstrate the ultrastrong coupling between the phonon (at 0.95 THz) in a MaPbI_3 film and the metallic bound states in the continuum (BICs) in Au metasurfaces. The Rabi splitting can be continuously tuned from 28% to 48.4% of the phonon frequency by adjusting the parameters (size, shape and period) of Au metasurfaces, reaching the ultrastrong coupling regime. By introducing wavelet transform, the mode evolution information of the terahertz phonon-polariton is successfully extracted. It indicates that the phonon radiation intensity of the MaPbI_3 film is enhanced as the coupling strength is increased. This work not only establishes a new platform for terahertz devices but also opens new avenues for exploring the intricate dynamics of terahertz phonon-polaritons.

Phonon-polariton is the quasi-particle generated from the interaction between light and phonons in materials, which is widely distributed from mid-infrared to terahertz (THz) ranges¹⁻⁵. It carries crucial physical information and exhibits potential applications, such as topological control⁶, tunable laser sources⁷ and thermal emitters². Notably, terahertz phonon-polariton is formed through the coupling of photons with THz phonons, which is a vital research focus within the realm of polaritons recently. Since the THz phonons widely exist in many prominent materials such as perovskites⁸, graphene⁵ and DNA molecules⁹, it can provide deep insights into these materials and crucial guidance for the design of terahertz sensors¹⁰ and detectors¹¹. Therefore, it is essential to develop a hybrid system for THz phonon-polaritons with an enhanced coupling strength. Especially for the hybrid system reaching the ultrastrong coupling regime¹², it transcends conventional physical limits and presents distinct physical phenomena, such as modified chemistry of molecules⁴, photon blockade¹³ and quantum gating effects¹⁴.

Most previous studies on terahertz phonon-polaritons are based on Fabry-Perot (F-P) cavities^{1,15-19} or plasmonic nanocavities²⁰⁻²⁴. Specifically, F-P cavities have a large mode volume with uniform local-field distributions, making it convenient for coupling with the thin films of organic molecules¹⁷ or crystalline semiconductor²⁵. However, the local-field enhancement in F-P cavities is moderate, leading to the limitation in achieving ultrastrong coupling strength. Furthermore, it is still challenging for miniaturization and integration. In contrast, plasmonic nanocavities offer a stronger local-field in a much smaller mode volume in nanostructures²⁶, thereby enhancing the coupling strength of the system. However, the typical mode volume of plasmonic nanocavities is much smaller than crystalline particles, such as MaPbI_3 ($\sim 300 \text{ nm}$)²⁷, α -lactose ($> 10 \mu\text{m}$)²⁸, leading to a spatial mismatching between the cavity and the phonon modes. As mentioned, both cavities show the limitations for further

enhancing the coupling strength of THz phonon-polaritons. Therefore, it is urgent to develop a new hybrid system for studying THz phonon-polaritons under the ultrastrong coupling regime.

In recent years, bound states in the continuum (BICs) have been actively studied in optical systems²⁹, accompanied by many discoveries and applications such as optical microcavities³⁰, lasers³¹ and sensors^{32,33}. BICs have been shown the excellent abilities for enhancing light-matter interactions³⁴, providing a strongly enhanced local-field, high quality factor (Q), ultrathin thickness, and broad resonance tunability via variation of their geometrical parameters^{29,35}. In particular, BICs can reduce thermal losses while simultaneously increasing coupling strength in the system of metallic metasurfaces³⁶. These capabilities make metallic metasurfaces based on BICs a promising platform for achieving and modulating ultrastrong coupling in the terahertz range. In addition, MaPbI_3 is a perovskite material with excellent optoelectronic properties, which shows potential applications in batteries³⁷, solar energy conversion³⁸, and light-emitting diodes (LEDs)³⁹. MaPbI_3 exhibits strong phonon vibrations at 0.95 THz, and can be easily crystallized into a high-quality crystalline film through spin-coating and thermal annealing making them a highly significant terahertz material that has attracted considerable attention^{38,40-42}. Therefore, MaPbI_3 is a suitable phonon material for THz phonon-polaritons.

Here, we report the demonstration of the ultrastrong coupling between the phonon in MaPbI_3 film and the metallic BICs in Au metasurfaces. The unit cell of the Au metasurface consists of the coupled C-shaped Au split ring resonator (SRR) pairs, forming the BIC modes. The resonance linewidth of BICs is controlled via the asymmetry of the unit cell, matching with the damping rate of phonon vibration. By varying the size of unit cells, the BIC resonance frequency is continuously tuned to match with the MaPbI_3 phonon frequency at 0.95 THz, and a Rabi splitting up to 0.28 THz is obtained.

Importantly, the Rabi splitting can further be tuned from 28% to 48.4% of the phonon frequency by precisely controlling the mode volume of BICs, reaching the ultrastrong coupling regime. By introducing wavelet transform, the mode evolution information of the terahertz phonon-polariton is successfully extracted. It indicates that the phonon radiation intensity of the MaPbI_3 film is enhanced as the coupling strength is increased. Our results open up new possibilities for the control of polaritons and reveal new information within the phonon-polaritons system.

Result

Sample design and BICs theory. Figure 1a illustrates the proposed hybrid system, which is composed of Au metasurface and MaPbI_3 film (see Method for details). Figure 1b shows the unit cell of the Au metasurface, it can be seen the asymmetric C-shaped Au SRR pairs, and the asymmetric degree can be controlled by the difference of arm lengths, $\Delta L = L_1 - L_2$. As the two electromagnetic modes in Au SRR pairs are coupled with each other, two new modes are generated. In special cases, one of these modes exhibits zero radiation loss, which is called BIC. The metallic BIC modes discussed in this paper can be elucidated using the Friedrich–Wintgen (F-W) BICs theory. In principle, BIC modes are analyzed by treating the metal as a perfect electric conductor (PEC), the simulated Q factor exhibits an inverse square relationship with ΔL as shown by the orange curve in Figure 1c. When $\Delta L = 0$, the Q factor of the BIC modes approaches infinity, because the loss associated with the metal is considered to be zero in the PEC model. When the Drude model is used to depict the refraction index of Au, the simulated Q factor of the BIC modes is shown by the blue curve in Figure 1c, which matches well with the PEC model when ΔL is large. However, as ΔL approaches zero, the Q factor is limited to below 200, because of the inherent losses of Au in the Drude model. The red stars in Figure 1c represent the experimental results of the Q factor which show a trend consistent with the

Drude model (see Method for experiment setup). The relationship approximately follows an inverse square proportionality with respect to ΔL . Due to factors such as uncertainties during the sample preparation, the measured Q values are lower than the simulated results under the Drude model at low asymmetry (See Supplementary Note 1).

MaPbI₃ is selected as the phonon material for the coupling system. In the classical model, the dielectric constant dispersion of phonon modes is typically described by Lorentz model. The relative permittivity can be expressed as:

$$\varepsilon_r = \varepsilon_\infty + \chi = \varepsilon_\infty - \frac{\omega_p^2}{\omega^2 - \omega_0^2 + i\omega\gamma} \quad (1)$$

where χ is the polarization susceptibility, ε_∞ is the permittivity at infinite frequency. $\omega_p^2 = \frac{ne^2}{\varepsilon_0 m}$, where ω_0 and γ represent the phonon frequency and damping rate. The refractive index is given by $n = \sqrt{\varepsilon_r}$ (Supplementary Note 2).

Strong coupling in Au-MaPbI₃ hybrid metasurfaces. As shown in Figure 2a, the BIC resonance peak is continuously tuned from 0.68 to 1.53 THz through the phonon frequency at 0.95 THz by adjusting the scaling factor S of the unit cell. S parameter is defined as the proportional magnified ratio in size in comparison with the standard size of the unit cell in Figure 1b. Noting that the asymmetric parameter is kept as the constant of $\Delta L = 34 \mu\text{m}$, when the resonance linewidth of the BIC mode is matched with the damping rate of the phonon. At this parameter of asymmetry, the Rabi splitting due to the coupling between the BICs and phonons is most pronounced (Supplementary Note 3). Figure 2b shows the position of the BIC resonance peak before (red dashed line) and after (red solid line) MaPbI₃ film coating. It shows a significant redshift after coating, due to the influence of the vacuum dielectric constant of MaPbI₃. At this stage, the MaPbI₃ film has not undergone annealing and

is in an intermediate phase, which exhibits no phonon resonance. Figure 2c shows the transmission amplitude of the crystallized MaPbI_3 film on a quartz substrate after thermal annealing. The quality of crystallization of perovskite significantly affects the coupling strength. The MaPbI_3 thin film has a thickness of approximately 200 nanometers and exhibits good crystallization quality, with a particle size significantly smaller than the minimum size of the metasurface unit cells. This allows for optimal coupling between the BICs and the phonons of MaPbI_3 (Supplementary Figure S12a).

After crystallization of the perovskite films on the Au metasurfaces, as shown in Figure 2d, the transmission amplitude of the system exhibits a pronounced anti-crossing feature. To explain the changes in modes before and after coupling between BICs and phonons, the variations in the energy levels of the system and the interactions between these energy levels were analyzed. From the Hamiltonian of the system, the energy levels and interactions that govern the dynamics of the coupled modes within the hybrid metasurfaces can be derived. The Hamiltonian can be expressed in the following form:

$$\hat{H} = \begin{pmatrix} \omega_{\text{BIC}} - i\gamma_{\text{BIC}} & g \\ g & \omega_{\text{Ph}} - i\gamma_{\text{Ph}} \end{pmatrix} \quad (2)$$

The energies of the upper and lower polariton branches can be calculated from

$$\omega_{\pm} = \frac{\omega_{\text{BIC}} + \omega_{\text{Ph}}}{2} + \frac{i(\gamma_{\text{BIC}} + \gamma_{\text{Ph}})}{2} \pm \sqrt{\left(g^2 - \frac{1}{4}(\gamma_{\text{BIC}} - \gamma_{\text{Ph}} + i(\omega_{\text{BIC}} - \omega_{\text{Ph}}))^2\right)} \quad (3)$$

where the resonance frequency of BIC and phonon are ω_{BIC} and ω_{Ph} , and damping rate of BIC and phonon are $\gamma_{\text{BIC}} = 0.18$ THz and $\gamma_{\text{Ph}} = 0.20$ THz, the properties of the BICs and phonons are extracted from measurement (Figures 2b and c). And g is the coupling strength between the two coupled elements. The corresponding Rabi splitting is defined as $\Omega_{\text{R}} = 2\sqrt{(g^2 - (\gamma_{\text{BIC}} - \gamma_{\text{Ph}})^2/4)}$.

As shown in Figure 2d, the interaction between the BICs and the phonons leads to a hybridization effect, resulting in the emergence of new resonant peaks that are characteristic of phonon-polaritons. The transmission amplitude shows clear anticrossing behaviour, which is an essential feature of strong coupling systems. It indicates that the BICs and phonons have strongly coupled to form new phonon-polariton modes. The transmission amplitude of the polariton modes shown in Figure 2d was analyzed according to Equation (3). The minimum of the splitting corresponds precisely to the condition where $\omega_{\text{BIC}} = \omega_{\text{Ph}} = 0.95$ THz (Figure 2e). This result indicates that the system's Rabi splitting is 0.28 THz, which is correspond to 1.15 meV. According to established criteria of strong coupling⁴³ $c = 2g/\sqrt{(\gamma_{\text{BIC}}^2 + \gamma_{\text{Ph}}^2)/2} > 1$, which leads to $c = 1.47 > 1$. Obviously, the experimental results substantially exceed the required conditions, confirming that the coupling strength of our Au-MaPbI₃ hybrid metasurfaces indeed reach the criteria of strong coupling. Furthermore, the experimental results align well with the simulation outcomes (Supplementary Figure S7), providing additional validation for our findings. The formation of these phonon-polariton modes enhances the light-matter interaction, leading to increased field localization and modified dispersion characteristics.

Tailoring the ultrastrong coupling in Au-MaPbI₃ hybrid metasurfaces. The general definition of Rabi splitting¹² is

$$\hbar\Omega_{\text{R}} = \hbar\Omega\sqrt{N} \propto \sqrt{\frac{N}{V_{\text{eff}}}} \quad (4)$$

where N is the number of oscillators participating in the coupling, and $\hbar\Omega$ represents the contribution from each oscillator. The mode volume is defined as $V_{\text{eff}} = \int \epsilon E^2 dV / \max(E^2)$, where E represents the electric field strength at various positions within the system.

In strong coupling systems, the coupling strength is increased as the mode volume of BIC decreases according to Equation (4). In situations where it is challenging to increase the maximum electric field strength, compressing the mode volume by reducing the period of the metasurface can effectively enhance the Rabi splitting. So, the metasurfaces are designed with different periods by varying the parameter $d = P_x - L_x$ to tune the coupling strength by changing the mode volume. A series of different parameters d from 50 to 2 μm are selected based on the metasurface with $d = 16 \mu\text{m}$ in Figure 2d. $P_y - L_y$ is scaled proportionally with d , while other geometrical parameters of the metasurface remain constant according to the structural parameters from Figure 1b. In this case, the resonance of the BIC modes can match with phonons, which are in the optimal position for generating phonon polaritons.

The transmission amplitude of the samples is shown in Figure 3a. When the period of the metasurface decreases as d increases from 16 to 50 μm , the Rabi splitting is modulated from 0.28 THz to 0.26 THz, indicating a slight change. When d is less than 16 μm , the Rabi splitting is significantly enhanced as d decreases. Specifically, as d is reduced from 16 to 2 μm , the Rabi splitting is modulated from 0.28 THz to 0.46 THz. As a result, the Rabi splitting of the phonon polariton is increased as d decreases, with a modulation range from 28% to 48.4% of the phonon frequency. By extracting the peak frequencies of two branches from each transmission spectrum, a linear relationship between Rabi splitting and $1/d$ can be fitted in Figure 3b. For metasurfaces, $V_{\text{eff}} \propto d^2$, substituting this into Equation (4) shows that the value of the Rabi splitting is inversely proportional to the square root of the mode volume. In addition, given that d is larger than the particle size observed after the crystallization of the MaPbI_3 , the number of participating phonons remains at saturation levels, which

means the influence of the number of phonons can be neglected. Therefore, it is sufficient only to focus on the relationship between the Rabi splitting and mode volume V_{eff} .

To obtain the tunability of the phonon-polariton in the metasurface with the maximum Rabi splitting, 5 samples are prepared based on the metasurfaces with $d = 2 \mu\text{m}$. The resonance of BIC modes is tuned from 0.7 to 1.2 THz by changing the scaling factor S . As shown in Figure 3c, the dots represent the peak frequencies of the upper and lower polariton branches obtained from the transmission amplitude of the samples. Clearly, anticrossing curves (dark curves in Figure 3c) were obtained by fitting with Equation (3), which means the frequency of phonon-polariton is tunable. The minimum frequency difference between the two polariton branches is 0.46 THz, occurring at the position where $\omega_{\text{BIC}} = \omega_{\text{Ph}}$. Consequently, the Rabi splitting produced by the sample is 48.4% of ω_{Ph} , placing the system well within the regime of ultrastrong coupling. This value represents one of the highest coupling strengths achieved in terahertz phonon-polariton systems to date.

Time evolution of electric model via wavelet analysis. Wavelet analysis yields the instantaneous spectrum for each delay in the mode evolution time trace, providing balanced results in both time and frequency domains. This method has emerged as a powerful tool for analyzing the temporal information of THz emission⁴⁴ and detection⁴⁵. To analyze the modes evolution of the generated phonon-polariton in this strong coupling system, THz fields passing through metasurfaces with representative periods are selected for the wavelet transform. As depicted in Figures 4a-d, the instantaneous spectrums of metasurfaces with four different parameters d are generated by wavelet analysis, which is performed with the generalized Morse wavelet⁴⁶ with $\beta = 120$, $\gamma = 3$ (Supplementary Note 5). The zero delay corresponds to the peak electric field of the terahertz wave prior to coupling with the material. The depth information in figures 4a-d represents the absolute amplitude of the

normalized THz field, showing the frequency distribution at different times as the THz wave passes through the metasurface. The amplitude of the THz field attenuates to zero in 10 ps, indicating the rapid decay time for the polariton modes. This observation aligns with the classical expression for mode evolution $Q = 2\pi t/2T = \omega_0 t/2$, where t represents the oscillator lifetime, consistent with the damping rate derived from the results in Figure 3a. The modes in the directly obtained time-frequency spectrum are not clear enough, due to the influence of THz waves that do not participate in coupling. Therefore, in Figures 4e and f, clear modes evolution spectrum of the phonon-polariton are obtained by subtracting the backgrounds of Figures 4b and d. The three highlighted areas in Figure 4e, from top to bottom represent the upper polariton branch, the phonon mode, and the lower polariton branch respectively. Figure 4f shows a similar result. The highlighted mode frequencies in Figures 4e and 4f correspond directly to the positions of the valley in the transmission amplitude spectrum in Figure 3a.

Notably, Figures 4e and f contain time evolution information of modes that cannot be obtained from the frequency domain spectrum through the Fast Fourier Transform (FFT). From the comparison of Figures 4e and f, it can be observed that the phonon mode appears 1.5 ps earlier as d decreases. To further analyze the reasons for the temporal variations of the phonon modes in different samples, as shown in Figures 5a and b, the intensity and phase evolution information at $\omega = 0.95$ THz are obtained by processing the time-frequency spectrums for different parameters d (details see Supplementary Figure S9). It is observed notable changes in the phase of THz field in Figure 5a. Specifically, both the THz field intensity and phase of phonon mode exhibit abrupt transitions, with the timing of these transitions occurring earlier as d decreases. Furthermore, the wavepacket after the transition is primarily attributed to phonon re-emission. By comparing the THz field intensity of the re-emitted

phonon portion in Figure 5b, it can be observed that the phonon radiation from the hybrid metasurface with parameter $d = 2 \mu\text{m}$ is 10 dB higher than that with $d = 50 \mu\text{m}$. It is concluded that as d decreases, the coupling strength increases, and the radiative intensity of the phonon increases by 10 dB. This highlights the essence of enhanced coupling strength, which involves maximizing the proportion of radiative losses in the presence of material dissipation while minimizing the proportion of absorption losses. Similarly, the phase of the upper and lower polariton branches is significantly changed evolved over time, which reveals the process of energy absorption and re-emission within strong coupling systems (Supplementary Figure S10). This behavior underscores the coherent coupling mechanism inherent in the phonon-polariton system, where the interactions between the phonons and the polaritons lead to the formation of these two modes.

Conclusion

In summary, we demonstrate the ultrastrong coupling in Au-MaPbI₃ hybrid metasurfaces based on metallic BICs. The Rabi splitting can be continuously adjusted from 28% to 48.4% of the phonon frequency by modifying the period of the Au metasurfaces, thus reaching the ultrastrong coupling regime. Through wavelet transform, we successfully extracted the mode evolution information of the terahertz phonon-polariton. It indicates that the phonon radiation intensity of the MaPbI₃ film is enhanced with increasing coupling strength. Our findings provide critical insights into the interaction between the metallic BICs and the phonons of perovskite. The methodologies and insights gained can be applied to explore multi-mode coupling phenomena across various platforms and materials. This research fosters the development of innovative photonic devices, and opens new pathways for future investigations into polaritons and strong coupling effects in the terahertz regime.

Methods

Sample fabrication. The Au metasurfaces, with a thickness of 200 nm, were fabricated on a quartz substrate using UV lithography and Electron Beam Evaporation (EBE). The prepared samples were subsequently subjected to treatment in an ultraviolet ozone cleaner to thoroughly eliminate surface organic contaminants. Perovskite thin films were created using the solution spin coating method (Supplementary Figure S11). A mixture of MAI and PbI_3 was dissolved in a solution of N, N-dimethylformamide (DMF) and dimethyl sulfoxide (DMSO) in a 1:1 ratio. The solution was stirred on a magnetic stirrer at 60°C for 12 hours until fully dissolved. The solution was then filtered to obtain the MAPbI_3 perovskite precursor solution. Then, 40 μL of the MAPbI_3 precursor solution was spin-coat onto the metasurface at 1000 rpm for the first 10 seconds, followed by 6000 rpm for the next 30 seconds. 100 μL of chlorobenzene was dispensed onto the surface quickly and evenly. After spin coating, the sample was placed on a hot plate and annealed at 100°C for 15 minutes to complete the perovskite thin film preparation about 250 nm (See SI Figure S12). Lead iodide (PbI_2) was purchased from the Tokyo Chemical Industry. Methylammonium iodide (MAI) was purchased from MaterWin company. N, N-Dimethylformamide (DMF), dimethyl sulfoxide (DMSO), and chlorobenzene (CB) were obtained from Aladdin.

Experiment setup. We conducted terahertz spectroscopy measurements using our independently developed terahertz time-domain spectroscopy (THz-TDS) system (Supplementary Figure S13), and obtained detailed information about the terahertz field through Fast Fourier Transform (FFT) and wavelet analysis. The THz-TDS system is driven by a Ti-sapphire femtosecond laser, which generates laser pulses with a duration of 35 fs, a repetition rate of 1 kHz, and a center wavelength of 800 nm. The femtosecond laser beam is split into two paths, used for terahertz generation and detection

respectively. We utilize efficient metallic spintronic emitters of ultra-broadband terahertz radiation to generate terahertz pulses based on the principle of ultrafast photoinduced spin currents⁴⁷. The emitted terahertz pulse is polarized in the y-direction in Figure 1b, and passes through the sample before simultaneously impinges on a ZnTe crystal with another femtosecond laser pulse, where the detection of the terahertz pulse is accomplished via the electro-optic effect. To eliminate the impact of water molecules in the air on the experiment, the portion of the test system through which terahertz waves propagate is filled with dry air maintained at a humidity level below 5%.

Data availability

The main data supporting the findings of this study are available within the article and its Supplementary Information files. Extra data are available from the corresponding author upon reasonable request.

Acknowledgements

This work was supported by National Key Research and Development Program of China (No. 2022YFA1604403) and National Natural Science Foundation of China (No. 12274157, No. 12021004, No. 12274334, No. 11904271), and Natural Science Foundation of Hubei Province of China (No. 2023AFA076). Special thanks are given to the Analytical and Testing Center of HUST and the Center of Micro-Fabrication and Characterization (CMFC) of WNLO for the use of their facilities.

Author contributions

K. W., P. X. L. conceived the project. K.W., P. X. L. supervised the project. J.X.Y., X. B. H. and F.R.L. designed the experiments. J.X.Y., A.Y.F. and C.Z. performed the experiments. J.X.Y., L.Y.Z. and X. B. H. performed theoretical calculations and numerical simulations. J.X.Y., L.Y.Z., K.W., A.Y.F.,

C.Z., Z.J.H., Z.D.L., X.B.H. analyzed data. All authors discussed the results. J.X.Y., C.Z., and L.Y.Z. drafted the paper with the inputs from all authors.

Competing interests

The authors declare no conflicts of interest.

References

1. Barra-Burillo, M. *et al.* Microcavity phonon polaritons from the weak to the ultrastrong phonon–photon coupling regime. *Nat. Commun.* **12**, 6206 (2021).
2. Lu, G. *et al.* Engineering the Spectral and Spatial Dispersion of Thermal Emission via Polariton–Phonon Strong Coupling. *Nano Lett.* **21**, 1831–1838 (2021).
3. Mekonen, S. M., Jain, D., Oh, S. & Armitage, N. P. Coupled Metamaterial–Phonon Terahertz Range Polaritons in a Topological Insulator. *ACS Photonics* **11**, 2242–2246 (2024).
4. Martínez-Martínez, L. A., Ribeiro, R. F., Campos-González-Angulo, J. & Yuen-Zhou, J. Can Ultrastrong Coupling Change Ground-State Chemical Reactions? *ACS Photonics* **5**, 167–176 (2018).
5. Epstein, I. *et al.* Far-field excitation of single graphene plasmon cavities with ultracompressed mode volumes. *Science* **368**, 1219–1223 (2020).
6. Kim, S. *et al.* Topological Control of 2D Perovskite Emission in the Strong Coupling Regime. *Nano Lett.* **21**, 10076–10085 (2021).
7. Ohtani, K. *et al.* An electrically pumped phonon-polariton laser. *Sci. Adv.* **5**, 1632 (2019).
8. La-o-vorakiat, C. *et al.* Phonon Mode Transformation Across the Orthorhombic–Tetragonal Phase Transition in a Lead Iodide Perovskite $\text{CH}_3\text{NH}_3\text{PbI}_3$: A Terahertz Time-Domain Spectroscopy Approach. *J. Phys. Chem. Lett.* **7**, 1–6 (2016).
9. Cheon, H., Yang, H., Lee, S.-H., Kim, Y. A. & Son, J.-H. Terahertz molecular resonance of cancer DNA. *Scientific Reports* **6**, 37103 (2016).
10. Odit, M. *et al.* Observation of Supercavity Modes in Subwavelength Dielectric Resonators. *Adv. Mater.* **33**, 2003804 (2021).

11. Wang, R. *et al.* Ultrasensitive Terahertz Biodetection Enabled by Quasi-BIC-Based Metasensors. *Small* **19**, 2301165 (2023).
12. Frisk Kockum, A., Miranowicz, A., De Liberato, S., Savasta, S. & Nori, F. Ultrastrong coupling between light and matter. *Nat. Rev. Phys.* **1**, 19–40 (2019).
13. Ridolfo, A., Leib, M., Savasta, S. & Hartmann, M. J. Photon Blockade in the Ultrastrong Coupling Regime. *Phys. Rev. Lett.* **109**, 193602 (2012).
14. Stassi, R., Cirio, M. & Nori, F. Scalable quantum computer with superconducting circuits in the ultrastrong coupling regime. *npj Quantum Inf.* **6**, 67 (2020).
15. Di Virgilio, L. *et al.* Controlling the electro-optic response of a semiconducting perovskite coupled to a phonon-resonant cavity. *Light Sci. Appl.* **12**, 183 (2023).
16. Ergoktas, M. S. *et al.* Topological engineering of terahertz light using electrically tunable exceptional point singularities. *Science* **376**, 184–188 (2022).
17. Damari, R. *et al.* Strong coupling of collective intermolecular vibrations in organic materials at terahertz frequencies. *Nat. Commun.* **10**, 3248 (2019).
18. Kim, H. S., Khan, A. A., Park, J.-Y., Lee, S. & Ahn, Y. H. Mechanical Control of Polaritonic States in Lead Halide Perovskite Phonons Strongly Coupled in THz Microcavity. *J. Phys. Chem. Lett.* **14**, 10318–10327 (2023).
19. Gao, W., Li, X., Bamba, M. & Kono, J. Continuous transition between weak and ultrastrong coupling through exceptional points in carbon nanotube microcavity exciton–polaritons. *Nature Photon.* **12**, 362–367 (2018).
20. Shelton, D. J. *et al.* Strong Coupling between Nanoscale Metamaterials and Phonons. *Nano Lett.* **11**, 2104–2108 (2011).
21. Jin, X. *et al.* Reshaping the phonon energy landscape of nanocrystals inside a terahertz plasmonic nanocavity. *Nat. Commun.* **9**, 763 (2018).
22. Jaber, A. *et al.* Hybrid architectures for terahertz molecular polaritonics. *Nat. Commun.* **15**, 4427 (2024).
23. Roh, Y. *et al.* Ultrastrong Coupling Enhancement with Squeezed Mode Volume in Terahertz Nanoslots. *Nano Lett.* **23**, 7086–7091 (2023).
24. Kim, H. S. *et al.* Phonon-Polaritons in Lead Halide Perovskite Film Hybridized with THz Metamaterials. *Nano Lett.* **20**, 6690–6696 (2020).

25. Bajoni, D. *et al.* Polariton Laser Using Single Micropillar GaAs – GaAlAs Semiconductor Cavities. *Phys. Rev. Lett.* **100**, 047401 (2008).
26. Zhang, Z. *et al.* Ultrastrong coupling between THz phonons and photons caused by an enhanced vacuum electric field. *Phys. Rev. Research* **3**, L032021 (2021).
27. Ding, J. *et al.* Design Growth of MAPbI₃ Single Crystal with (220) Facets Exposed and Its Superior Optoelectronic Properties. *J. Phys. Chem. Lett.* **9**, 216–221 (2018).
28. Patel, S. R. & Murthy, Z. V. P. Effect of process parameters on crystal size and morphology of lactose in ultrasound-assisted crystallization. *Cryst. Res. Technol.* **46**, 243–248 (2011).
29. Hsu, C. W., Zhen, B., Stone, A. D., Joannopoulos, J. D. & Soljačić, M. Bound states in the continuum. *Nat. Rev. Mater.* **1**, 16048 (2016).
30. Wang, W., Srivastava, Y. K., Tan, T. C., Wang, Z. & Singh, R. Brillouin zone folding driven bound states in the continuum. *Nat. Commun.* **14**, (2023).
31. Che, Y. *et al.* Ultrasensitive Photothermal Switching with Resonant Silicon Metasurfaces at Visible Bands. *Nano Lett.* **24**, 576–583 (2024).
32. Tan, T. C. *et al.* Active Control of Nanodielectric-Induced THz Quasi-BIC in Flexible Metasurfaces: A Platform for Modulation and Sensing. *Adv. Mater.* **33**, 2100836, (2021).
33. Ren, Z. *et al.* Overcoming High-Quality Limitations in Plasmonic Metasurfaces for Ultrasensitive Terahertz Applications. *ACS Nano* **18**, 21211–21220 (2024).
34. Weber, T. *et al.* Intrinsic strong light-matter coupling with self-hybridized bound states in the continuum in van der Waals metasurfaces. *Nat. Mater.* **22**, 970–976 (2023).
35. Kang, M., Liu, T., Chan, C. T. & Xiao, M. Applications of bound states in the continuum in photonics. *Nat. Rev. Phys.* **5**, 659–678 (2023).
36. Liang, Y., Tsai, D. P. & Kivshar, Y. From Local to Nonlocal High-Q Plasmonic Metasurfaces. *Phys. Rev. Lett.* **133**, 053801 (2024).
37. Koh, T. M. *et al.* Formamidinium tin-based perovskite with low E_g for photovoltaic applications. *J. Mater. Chem. A* **3**, 14996–15000 (2015).
38. Liu, J. *et al.* Electron injection and defect passivation for high-efficiency mesoporous perovskite solar cells. *Science* **383**, 1198–1204 (2024).
39. Kojima, A., Teshima, K., Shirai, Y. & Miyasaka, T. Organometal Halide Perovskites as Visible-Light Sensitizers for Photovoltaic Cells. *J. Am. Chem. Soc.* **131**, 6050–6051 (2009).

40. Zhizhchenko, A. *et al.* Single-Mode Lasing from Imprinted Halide-Perovskite Microdisks. *ACS Nano* **13**, 4140–4147 (2019).
41. Zhizhchenko, A. Y. *et al.* Light-Emitting Nanophotonic Designs Enabled by Ultrafast Laser Processing of Halide Perovskites. *Small* **16**, 2000410 (2020).
42. Onoda-Yamamuro, N., Matsuo, T. & Suga, H. Dielectric study of $\text{CH}_3\text{NH}_3\text{PbX}_3$ (X = Cl, Br, I). *Journal of Physics and Chemistry of Solids* **53**, 935–939 (1992).
43. Zhang, L., Gogna, R., Burg, W., Tutuc, E. & Deng, H. Photonic-crystal exciton-polaritons in monolayer semiconductors. *Nat. Commun.* **9**, 713 (2018).
44. Guzelturk, B. *et al.* Terahertz Emission from Hybrid Perovskites Driven by Ultrafast Charge Separation and Strong Electron–Phonon Coupling. *Adv. Mater.* **30**, 1704737 (2018).
45. Luo, T. *et al.* Time-of-flight detection of terahertz phonon-polariton. *Nat. Commun.* **15**, 2276 (2024).
46. Olhede, S. C. & Walden, A. T. Generalized Morse wavelets. *IEEE Trans. Signal Process.* **50**, 2661–2670 (2002).
47. Seifert, T. *et al.* Efficient metallic spintronic emitters of ultrabroadband terahertz radiation. *Nature Photon.* **10**, 483–488 (2016).

Captions

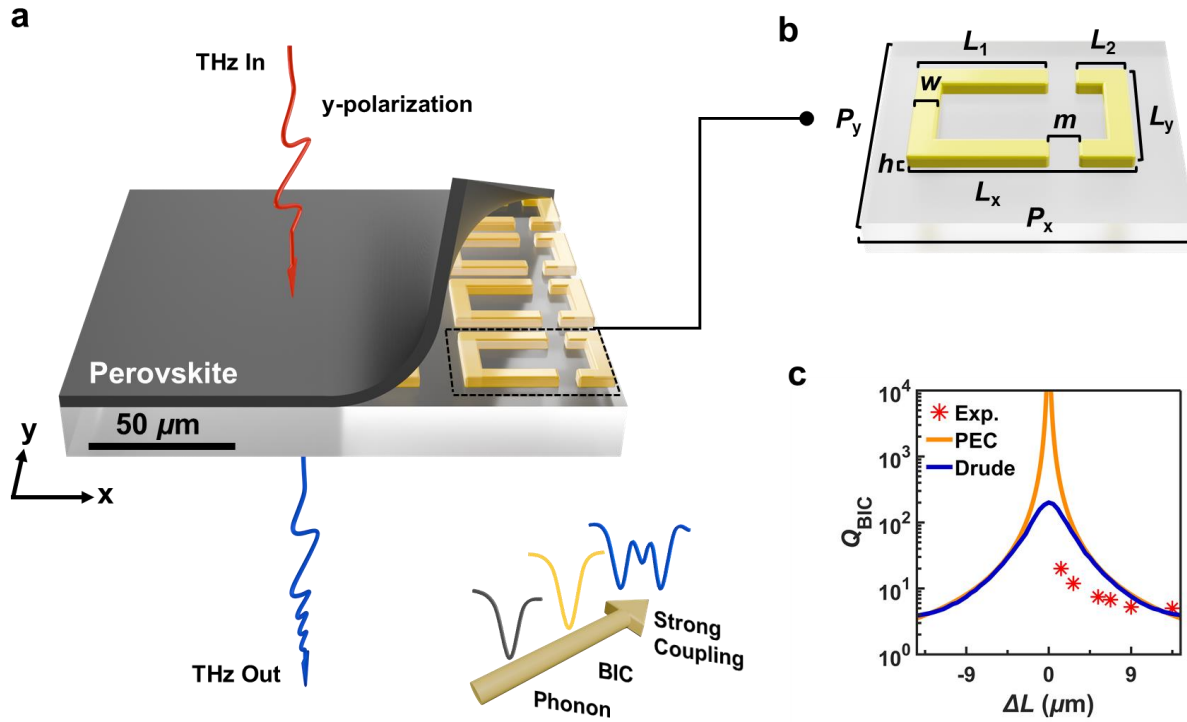


Figure 1 | **a**, Illustration of Au metasurfaces covered with a MaPbI_3 thin film. **b**, The structure of the BIC unit. The geometrical unit cell parameters are: $P_x = 66 \mu\text{m}$, $P_y = 32 \mu\text{m}$, $L_x = 50 \mu\text{m}$, $L_y = 25 \mu\text{m}$, $L_1 = 39.5 \mu\text{m}$, $m = 5 \mu\text{m}$, $w = 5 \mu\text{m}$, $h = 200 \text{ nm}$, with the period $d = P_x - L_x$. The tuning of the resonance position of the BIC modes is realized by introducing multiplicative scaling factor S , which scales the geometrical parameters of metasurfaces by multiplying all parameters by S . Terahertz waves pass through the sample in y-polarization and emerge from the quartz substrate side. (bottom right) Schematic diagram of strong coupling between phonons and BICs. **d**, Quality factor (Q) of the BIC modes varies with the degree of asymmetry. Red stars represent experimental data, while blue crosses represent the Drude model results, and simulations using parameters employed in the experiment. The orange solid line represents the ideal PEC case. The degree of asymmetry is defined by the expression $\Delta L = L_1 - L_2$.

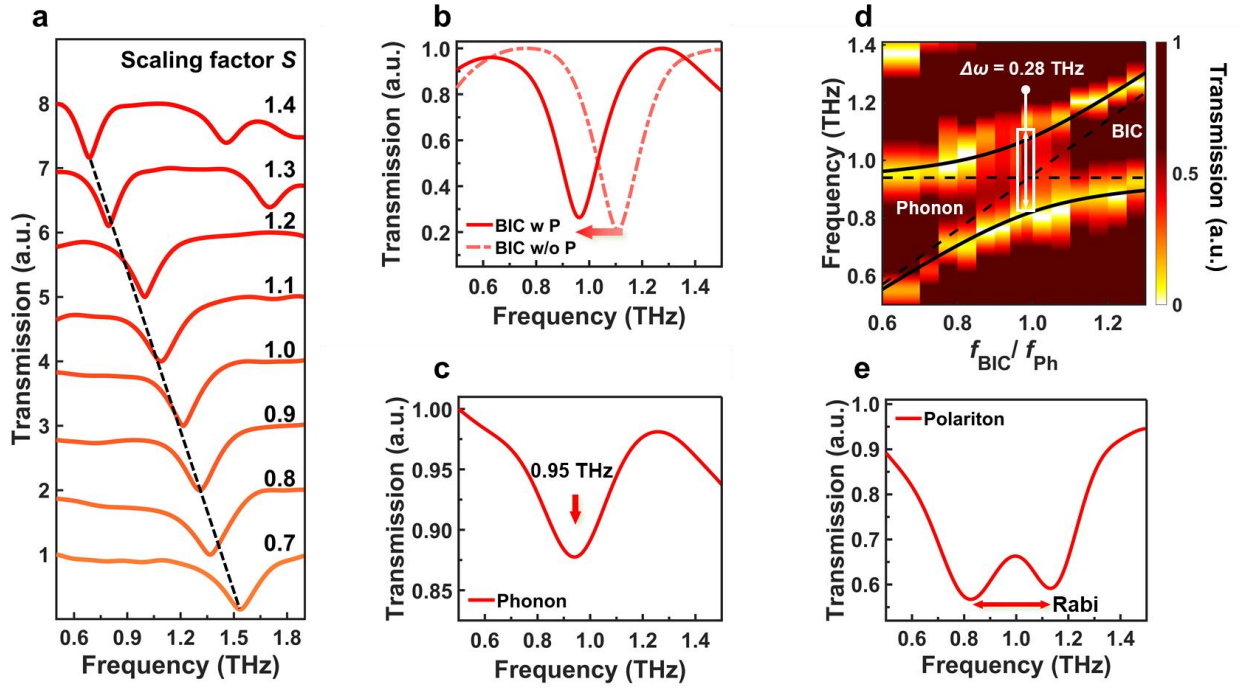


Figure 2 | **a**, Measured transmission amplitudes of BIC resonances across the frequency of perovskite phonon tuned via scaling the in-plane geometric parameters. The new parameters were derived by multiplying S with the in-plane geometric parameters. $P_{x\text{new}} = SP_x$, $P_{y\text{new}} = SP_y$, $L_{x\text{new}} = SL_x$, $L_{y\text{new}} = SL_y$, $L_{1\text{new}} = SL_1$, $m_{\text{new}} = Sm$, $w_{\text{new}} = Sw$. **b**, Transmission amplitude of the Au metasurface coated with an amorphous perovskite film is represented by red solid line, while that of pure Au metasurface without perovskite is represented by a red dashed line. **c**, The transmission amplitude of a MaPbI_3 film spin-coated on a quartz substrate. The arrow indicates the frequency of phonon resonance. **d**, Transmission amplitude of Au- MaPbI_3 metasurfaces for different scaling factors shows a characteristic and anticrossing mode pattern close to the MaPbI_3 phonon. **e**, Transmission amplitude of Au metasurface coated with a crystallized perovskite film while the resonance position of BICs is tuned to 0.95 THz, which reveals a Rabi splitting of 0.28 THz.

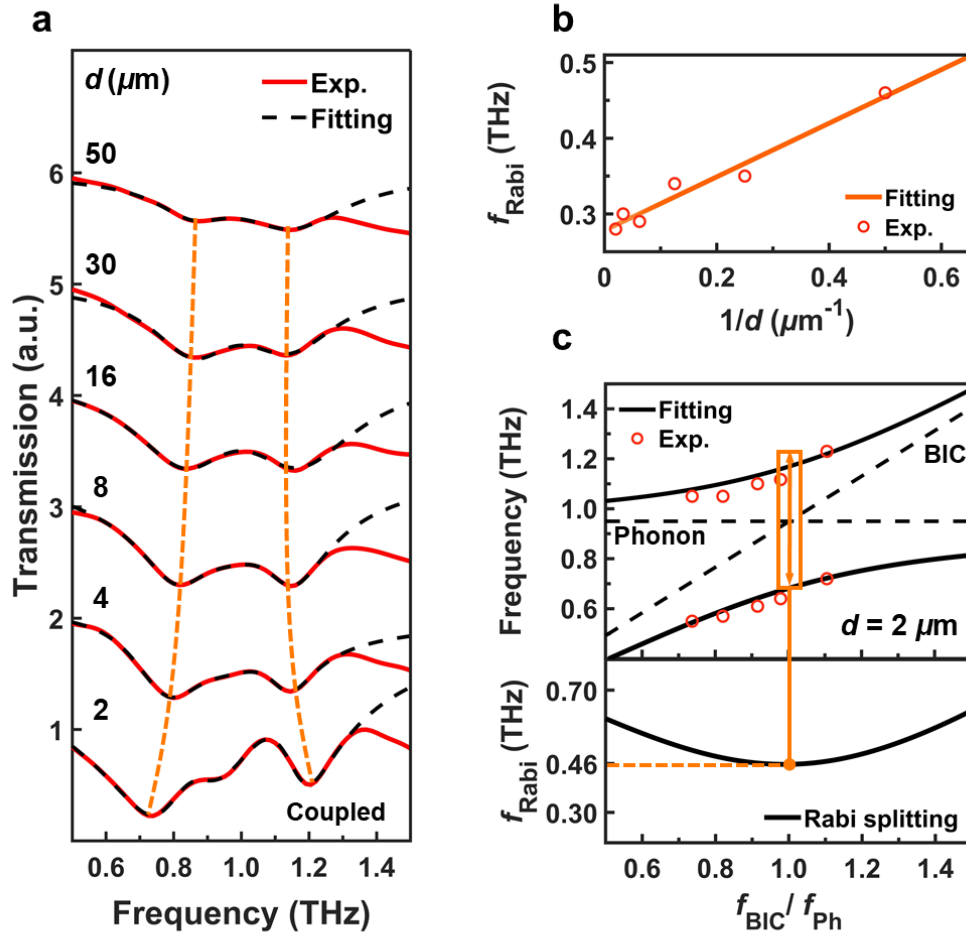


Figure 3 | **a**, Transmission amplitude that corresponds to the on-resonance case with the period d changed, where $L_x = 50 \mu\text{m}$ is constant. The red curve represents the experimental data, while the dark dashed line corresponds to the fit obtained from Equation (S8). The peaks of polariton are connected by orange dashed lines. **b**, Rabi splitting as a function of $1/d$. The red circles are the Rabi splitting of different d . The dark curve indicates a linear relationship between Rabi splitting and the inverse of d . **c**, Polariton peak positions (red circles) and the fitting dispersion predicted by the two-oscillator model (dark curves) for $d = 2 \mu\text{m}$. The position of the orange line is 0.95 THz.

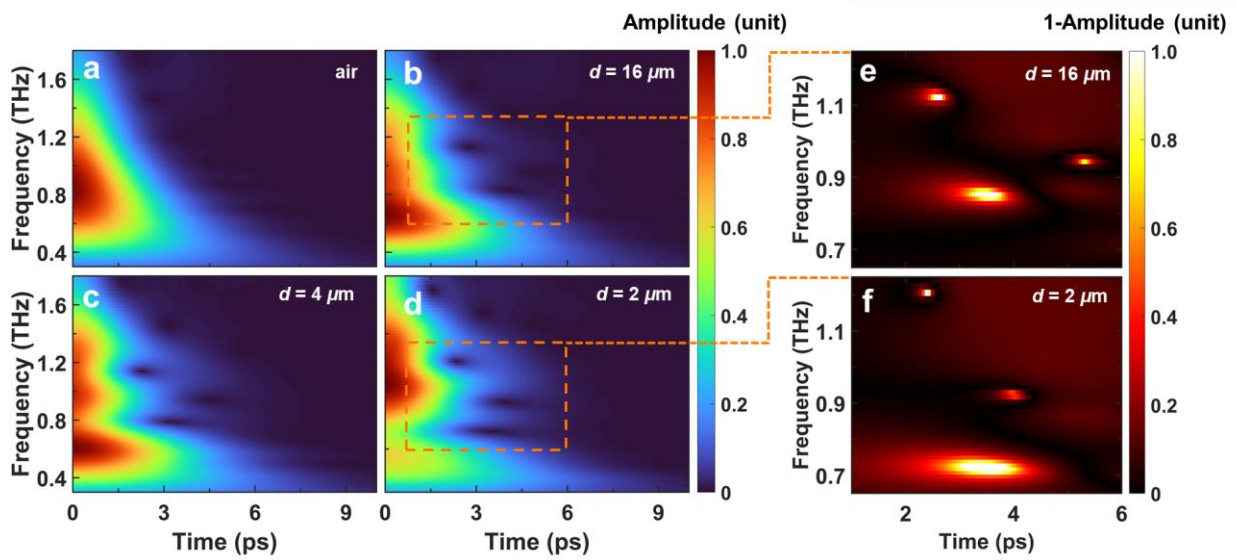


Figure 4 | **a-d**, Time-evolved spectrum obtained through the wavelet transform method. **(a)** without samples, **(b)** $d = 16 \mu\text{m}$, **(c)** $d = 4 \mu\text{m}$, **(d)** $d = 2 \mu\text{m}$. **e-f**, Time-frequency domain maps of the regions $d = 16 \mu\text{m}$ and $2 \mu\text{m}$ after background removal within the orange dashed boxes.

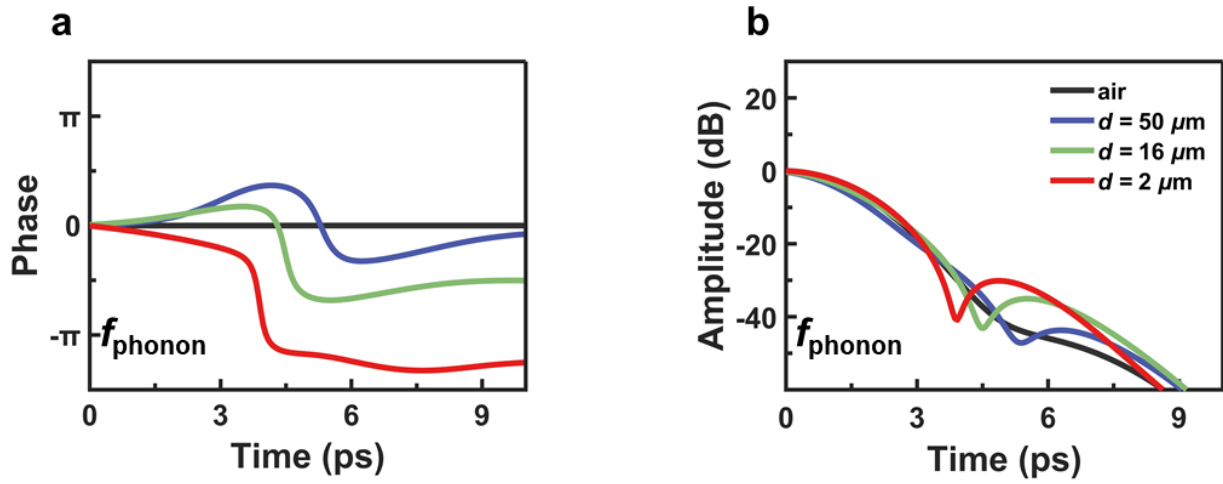


Figure 5 | Time evolution of (a) intensity and (b) phase of the terahertz field at $\omega_{\text{ph}} = 0.95$ THz for different d parameters.

Supplementary information

Manipulating terahertz phonon-polariton in the ultrastrong coupling regime with bound states in the continuum

Jiaying Yang¹, Kai Wang^{1,2}, Liyu Zhang¹, Chen Zhang¹, Aoyu Fan³, Zijian He¹, Zhidi Li¹,*

Xiaobo Han⁴, Furi Ling^{3}, Peixiang Lu^{1,4*}*

¹Wuhan National Laboratory for Optoelectronics and School of Physics, Huazhong University of Science and Technology, Wuhan 430074, China

²School of Electronic and Information Engineering, Hubei University of Science and Technology, Xianning 437100, China

³School of Optics and Electronic Information, Huazhong University of Science and Technology, Wuhan, Hubei 430074, P.R. China

⁴Hubei Key Laboratory of Optical Information and Pattern Recognition, Wuhan Institute of Technology, Wuhan 430205, China

*Corresponding authors:

kale_wong@hust.edu.cn (KW), lingfuri@mail.hust.edu.cn (FRL), lupeixiang@hust.edu.cn (PXL)

Contents:

Supplementary Note 1: Formation of metallic BIC

Supplementary Note 2: Drude-Lorentz model for perovskite phonon

Supplementary Note 3: Temporal coupled mode theory for strong coupling

Supplementary Note 4: Temporal coupled mode theory for time domain signal

Supplementary Note 5: Wavelet transform

Supplementary Note 6: Evolution of phonon-polariton

Supplementary Note 7: Sample fabrication

Supplementary Note 8: Experiment setup

Supplementary Note 1: Formation of metallic BIC

Figure S1a shows the eigenmode of the arrays of single C-shaped split ring resonator (SRR). The field intensity is stronger at the outer edges, especially at the endpoints of the SRR, which facilitates the coupling of modes depicted in Figure S2. As shown in Figure S1b, when the arm length L_1 decreases, the eigenfrequency increases linearly, while the loss is approximately constant.

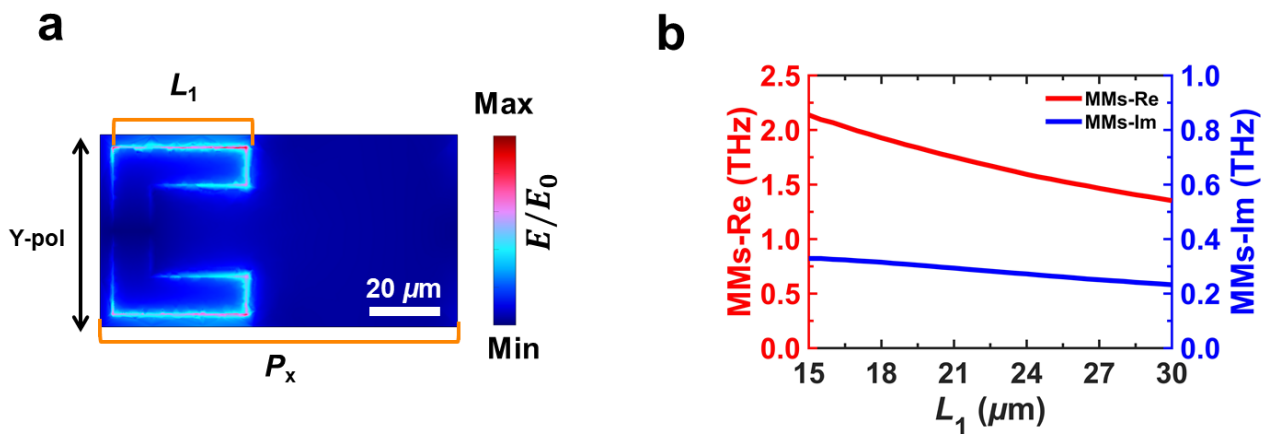


Figure S1 | **a**, The electric field distribution of the eigenmode of SRR. **b**, Eigenfrequency of the eigenmode of different arm lengths.

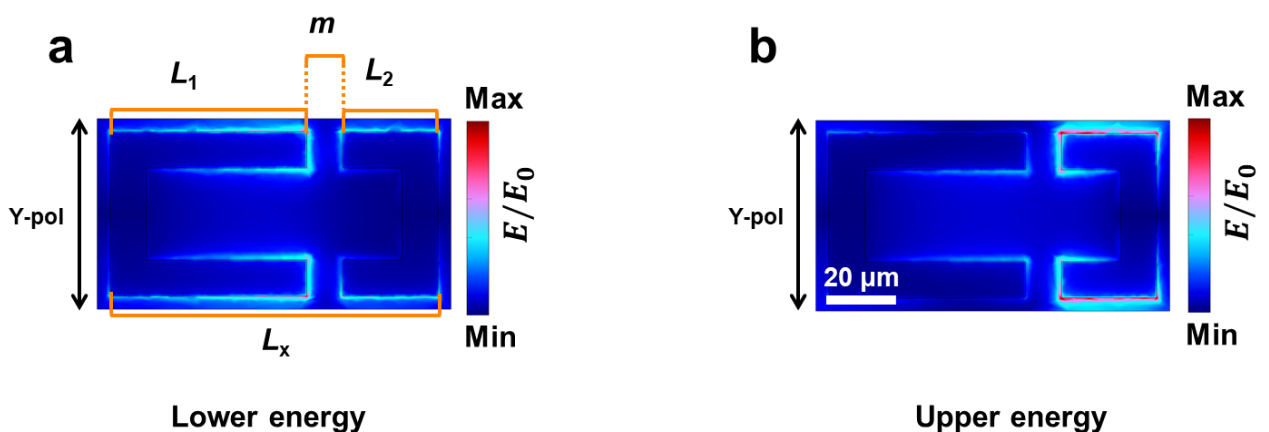


Figure S2 | **a-b**, The electric field distribution of the two generated eigenmodes in the asymmetrical metasurfaces.

(a) lower branch, (b) upper branch.

Next, two C-shaped SRRs are placed opposite to each other, the modes are coupled by nearfield. The gap length m between them is fixed to ensure the coupling between the two modes remains relatively constant. Figures S2a and b depict the field distributions of the low-frequency mode (lower band) and the high-frequency mode (upper band) on the left and the right respectively. It is noted that the field intensity of the low-frequency mode primarily concentrates on one side of the structure with the longer arms, while the high-frequency mode exhibits the opposite behavior.

The coupling of two modes in the unit of the metasurface can be elucidated through a Hamiltonian^{1,2},

$$H = \begin{pmatrix} \omega_1 - i\gamma_{1i} & \kappa \\ \kappa & \omega_2 - i\gamma_{2i} \end{pmatrix} - i \begin{pmatrix} \gamma_{1r} & \sqrt{\gamma_{1r}\gamma_{2r}} \\ \sqrt{\gamma_{1r}\gamma_{2r}} & \gamma_{2r} \end{pmatrix} \quad (S1)$$

where κ is the interaction potential between the two modes, ω_1, ω_2 are the resonant frequencies, γ_{1i}, γ_{2i} and γ_{1r}, γ_{2r} are nonradiative and radiative damping rates of the two modes respectively, $\sqrt{\gamma_{1r}\gamma_{2r}}$ represents the interference of radiation.

When metal is treated as perfect electric conductor (PEC), the non-radiative damping rate is zero.

The eigenfrequencies of the two new hybrid modes are

$$\omega_{u,d} = [\omega_1 + \omega_2 + i(\gamma_{1r} + \gamma_{2r})]/2 \pm \sqrt{\left(\frac{\omega_1 + \omega_2 + i(\gamma_{1r} + \gamma_{2r})}{2}\right)^2 + [\kappa^2 - \omega_1\omega_2 + i(\gamma_{2r}\omega_1 + 2\kappa\sqrt{\gamma_{1r}\gamma_{2r}} + \gamma_{1r}\omega_2)]} \quad (S2)$$

Therefore, when

$$\kappa(\gamma_{1r} - \gamma_{2r}) = \sqrt{\gamma_{1r}\gamma_{2r}}(\omega_1 - \omega_2) \quad (S3)$$

one eigenvalue is real and the eigenmode turns into a BIC, while the damping rate of the other eigenmode doubles. Apparently, when the unit has side-to-side symmetry, Equation (S3) holds.

Figures S3a and b illustrate the eigenmode analysis, where the metal is considered as PEC. The theory and simulations are in good agreement. The eigenfrequencies exhibit an anticrossing behavior,

and the damping rate of the lower modes approaches zero at the high symmetry point. This coupling behavior has been experimentally validated in Figure S3c.

Figures S4a and b correspond to the evolution of the mode's Q -factor in parameter space when considering the metal as PEC and as Drude-Lorentz material³. The asymmetry parameter is defined by⁴

$$\delta = \frac{L_1 - L_2}{L_1} \quad (\text{S4})$$

When radiation losses are significant, absorption losses can be neglected. However, when the lower branch mode approaches BIC, absorption losses must be taken into account. For PEC, this mode's Q -factor can exceed 10^5 , whereas with the Drude model, the Q -factor peaks around 200. Near this high-symmetry point, radiation loss follows a parabolic trend, while the Q -factor adheres to the well-known inverse square relationship.

$$Q = \omega/2\gamma$$

$$Q(\delta) \propto \delta^{-2} \quad (\text{S5})$$

This phenomenon can be observed in the experiment in Figure S4c.

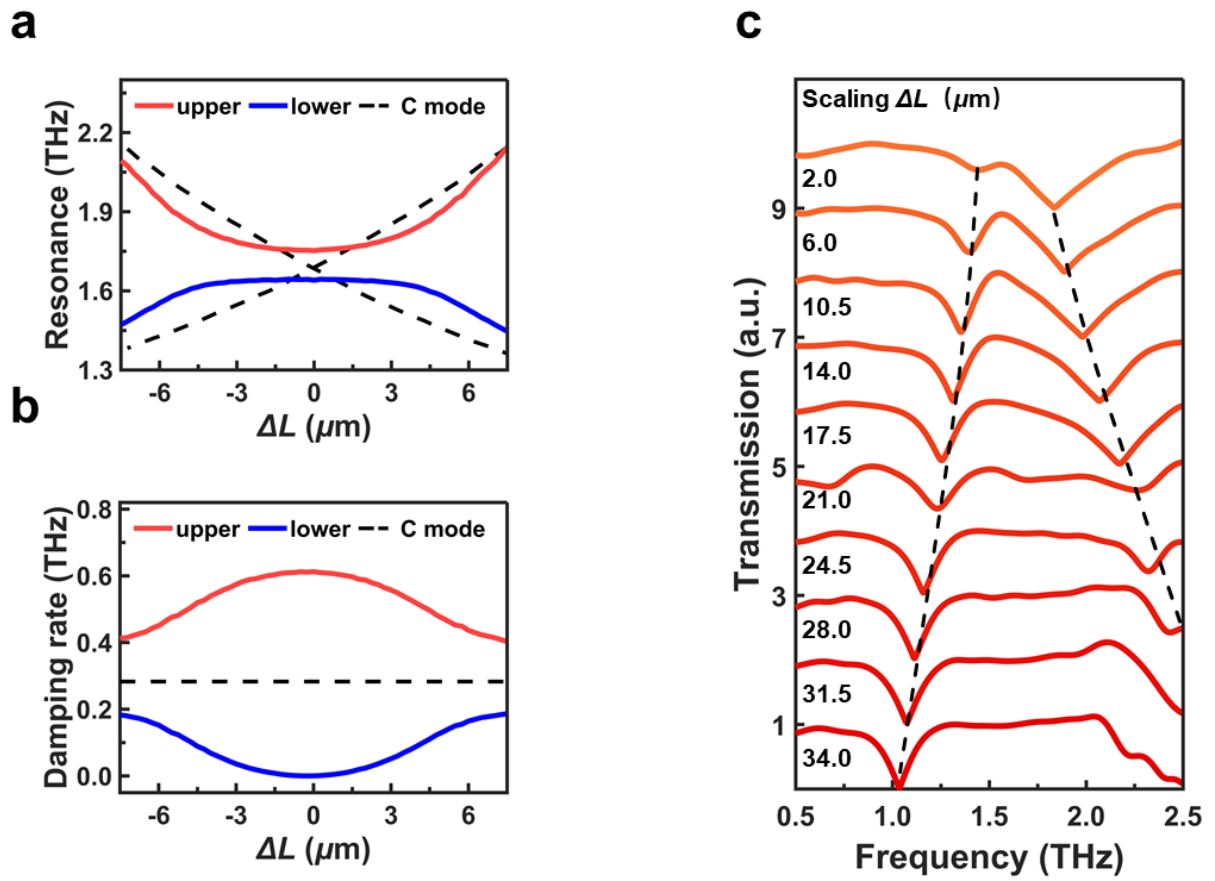


Figure S3 | a-b, The effect of coupling on the resonant frequencies and losses of two eigenmodes in simulation. **(a)** Resonant frequencies **(b)** Losses. **c,** The effect of coupling on the resonant frequencies and losses of two modes in the experiment.

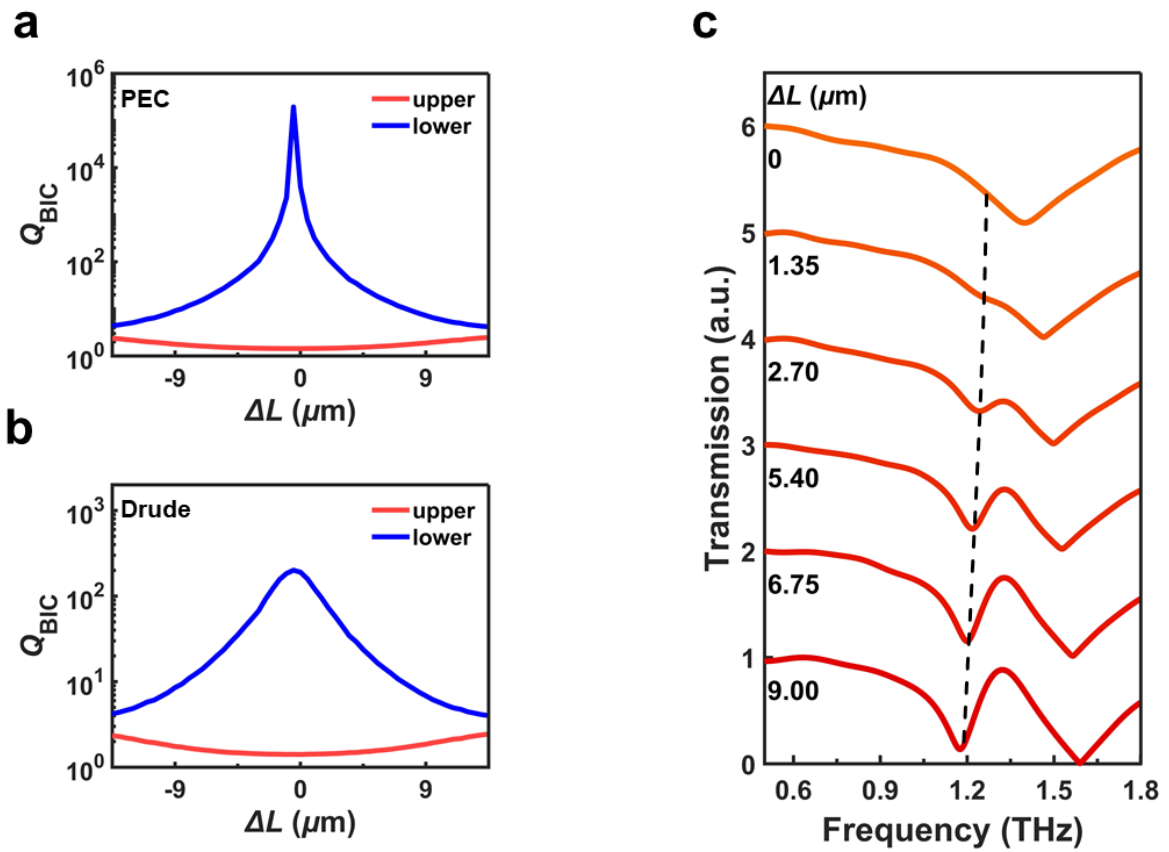


Figure S4 | **a-b**, Simulated Q factor of the BIC mode varies with the degree of symmetry breaking. **(a)** metal as PEC, **(b)** metal as Drude-Lorentz material. **c**, Transmission amplitudes for different symmetry-broken BIC metasurfaces.

Supplementary Note 2: Drude-Lorentz model for perovskite phonon

We utilize the Drude-Lorentz model with two poles to describe the phonons in perovskites⁵,

$$\varepsilon(\omega) = \varepsilon_{\infty} + \sum_{k=1}^2 \frac{f_k}{\omega_k^2 - \omega^2 - i\omega\gamma_k} \quad (\text{S6})$$

where f_k is the oscillator strength, ε_{∞} the background permittivity, ω_k the resonance frequency and γ_k the damping rate. The formula can be expressed in an equivalent form:

$$\varepsilon(\omega) = \varepsilon_{\infty} + \sum_{j=1}^2 \left(\frac{A_j}{\omega - \Omega_j} - \frac{A_j^*}{\omega - \Omega_j^*} \right) \quad (\text{S7})$$

where A_j is the residue at pole Ω_j .

In temporal coupled mode theory (TCMT), electromagnetic modes are also first-order poles of the response function, highlighting the similarity between phonon and electromagnetic modes.

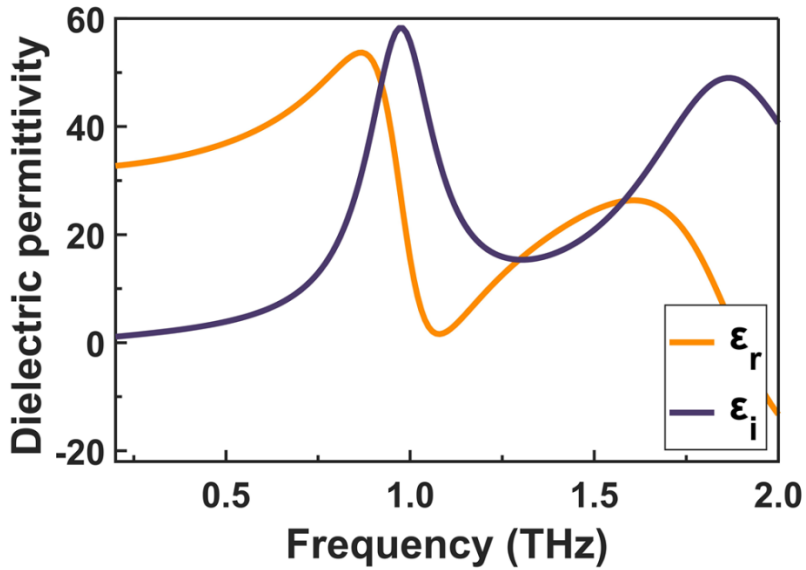


Figure S5 | The dielectric permittivity of MaPbI₃ using the Lorentz model.

Supplementary Note 3: Temporal coupled mode theory for strong coupling

Note 1 shows that the coupling of electromagnetic modes can be depicted by TCMT. Note 2 highlights the similarity between phonon and electromagnetic modes. In this section, TCMT is used to describe the strong coupling of phonon and BIC⁶. The experimental results presented in Figure 3a can be well fitted by Equation (S8).

The system is described by the scattering matrix S , and decays through ports 1 and 2. The resonance frequencies and intrinsic damping rates of the modes of the cavity are given by Ω and the radiative damping rates by Γ . The port-cavity coupling is described by K , which is a function of the radiative damping rates. The direct port-port crosstalk by the unitary matrix C .

$$S = C + K[i(\omega I - \Omega) + \Gamma]^{-1}K^T$$

$$\Omega = \begin{bmatrix} \omega_{\text{BIC}} + i\gamma_{\text{BIC,dis}} & g & 0 \\ g & \omega_{\text{Ph}} + i\gamma_{\text{Ph,dis}} & 0 \\ 0 & 0 & \omega_{\text{Ph}} + i\gamma_{\text{Ph,dis}} \end{bmatrix}$$

$$\Gamma = \begin{bmatrix} \gamma_{\text{BIC,rad}} & 0 & \sqrt{\gamma_{\text{BIC,rad}}\gamma_{\text{Ph,rad}}} \\ 0 & 0 & 0 \\ \sqrt{\gamma_{\text{BIC,rad}}\gamma_{\text{Ph,rad}}} & 0 & \gamma_{\text{Ph,rad}} \end{bmatrix}$$

$$K = \begin{bmatrix} \sqrt{\gamma_{\text{BIC,rad}}} & 0 & \sqrt{\gamma_{\text{Ph,rad}}} \\ \sqrt{\gamma_{\text{BIC,rad}}} & 0 & \sqrt{\gamma_{\text{Ph,rad}}} \end{bmatrix} e^{i\phi}$$

$$C = \begin{bmatrix} r_0 & it_0 \\ it_0 & r_0 \end{bmatrix}$$

$$e^{2i\phi} = -r_0 - it_0 \tag{S8}$$

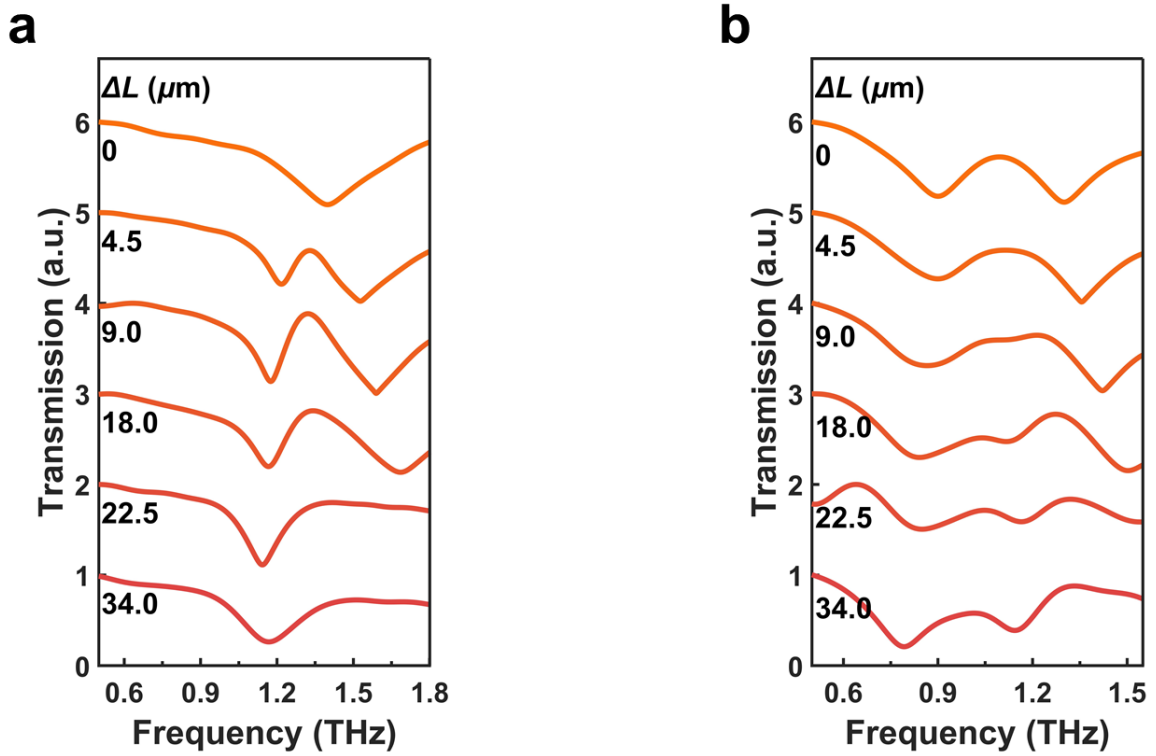


Figure S6 | **a-b**, Transmission amplitude of the metasurfaces under different symmetry-breaking conditions in the experiment. **(a)** without MaPbI_3 , **(b)** with MaPbI_3 .

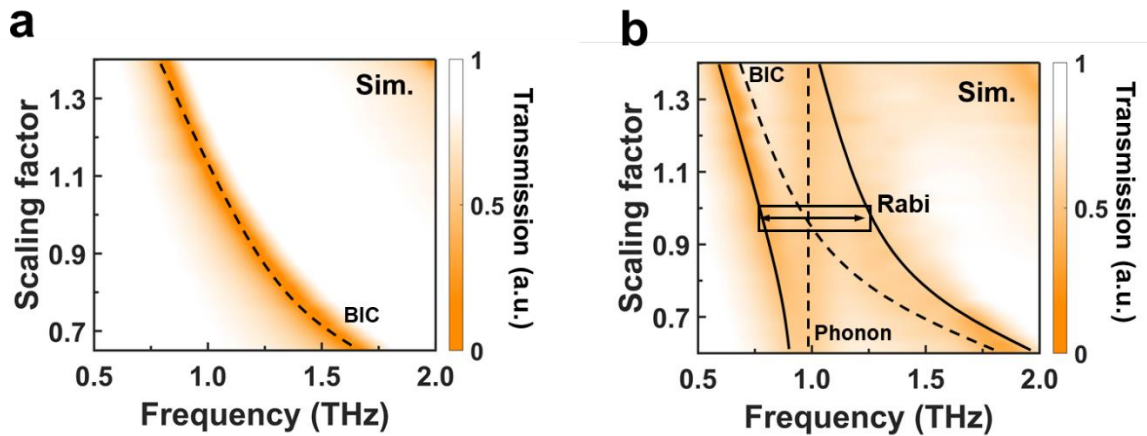


Figure S7 | **a**, Simulated transmittance amplitude of BIC resonances close to perovskite phonon tuned via scaling the in-plane geometric parameters. **b**, Simulated transmittance amplitude of BIC- MaPbI_3 metasurfaces for different scaling factors.

To investigate the influence of BIC asymmetry on Rabi splitting, a series of samples with different degrees of structural asymmetry ΔL are simulated and fabricated. The resonance of the BICs is aligned with that of the phonon by adjusting the scaling factor S . From the results in Figure S6b, it is evident that at low asymmetry levels, the coupling is significantly affected by the presence of another electric dipole mode in the structure, making it difficult to discern whether the BICs and phonons are coupled. However, when the asymmetry reaches $\Delta L = 9 \mu\text{m}$, the Rabi splitting of the phonon-polariton becomes clear and is unchanged as the degree of asymmetry increases. This behavior can be attributed to the fact that the intrinsic losses of the metal are substantial at low asymmetry, which means that reducing the degree of asymmetry does not significantly enhance the localized electric field strength in the metallic metasurfaces. Compared to PEC, the enhancement of the electric field in the Au metasurfaces is strongly limited by intrinsic losses. Therefore, due to the intrinsic losses associated with the metal, reducing the asymmetry of the BIC structures does not lead to a significant enhancement in Rabi splitting, but the criteria of strong coupling¹¹ $c = 2g/\sqrt{(\gamma_{\text{BIC}}^2 + \gamma_{\text{Ph}}^2)/2}$ is turned from 1.40 to 2.24.

The simulations presented in this paper employ a frequency domain solver, primarily based on the wave optics module of COMSOL Multiphysics. The structural parameters used in the simulations, as illustrated in Figure S7, are identical to those utilized in the experimental configurations. The geometrical unit cell parameters are: $P_x = 66 \mu\text{m}$, $P_y = 32 \mu\text{m}$, $L_x = 50 \mu\text{m}$, $L_y = 25 \mu\text{m}$, $L_1 = 39.5 \mu\text{m}$, $m = 5 \mu\text{m}$, $w = 5 \mu\text{m}$, $h = 200 \text{ nm}$. The metal conductivity is set to $\sigma = 6 \times 10^7 \text{ S/m}$.

Supplementary Note 4: Temporal coupled mode theory for time domain signal

Since the experiment measures signals in the time domain, it is essential not only to analyze the frequency-domain transmission but also to directly predict the time-domain signals using TCMT⁷⁻⁹.

$$\frac{da}{dt} = i\Omega a + KS_+ \quad (\text{S9})$$

where Ω is a N-dimensional diagonal matrix that represents the resonance frequency and damping rate, a represents the resonance amplitudes and is normalized, S_+ is the incoming wave, K is a coupling matrix.

$$S_- = CS_+ + Da \quad (\text{S10})$$

where C is direct scattering coefficient, D is another coupling matrix, S_- is outgoing wave. Once the incident light wave and a are determined, the outgoing wave can be directly obtained from Equation (S10). Given the initial conditions, Equation (S9) can be solved.

$$a_n(0) = 0 \quad (\text{S11})$$

$$a_n(t) = e^{i\Omega t} \int_0^t e^{i\Omega t'} K_n S_+(t') dt' \quad (\text{S12})$$

The coupling matrix obeys the following relations

$$D^\dagger D = \Gamma_r \quad (\text{S13})$$

$$K = D \quad (\text{S14})$$

$$CD^* = -D \quad (\text{S15})$$

where Γ_r is the radiative rate matrix.

Given the mode information, the outgoing wave can be calculated from the incident wave.

Supplementary Note 5: Wavelet transform

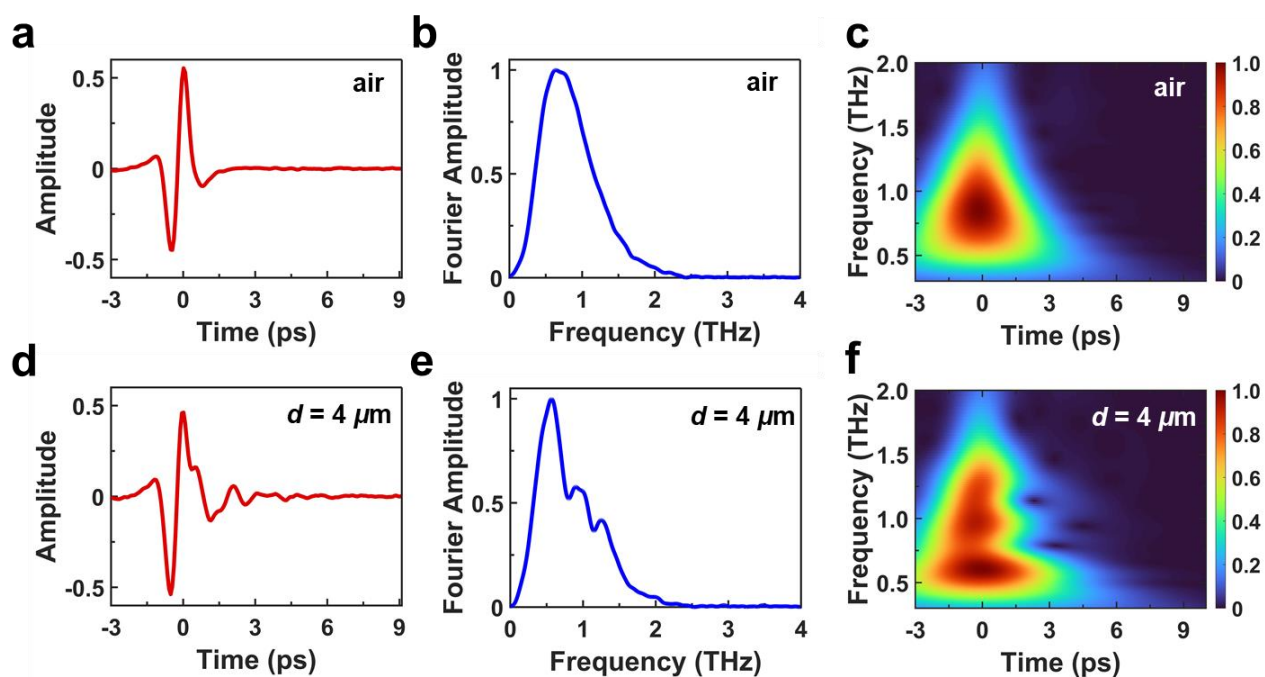


Figure S8 | **a**, The profile of the terahertz field without a sample. **b**, The spectrum of the terahertz through direct Fourier transform from the terahertz field in **(a)**. **c**, The time-frequency spectrum obtained through wavelet transform from the terahertz field in **(a)**. **d**, The terahertz field transmitted through a sample with a parameter of $d = 4 \mu\text{m}$. **e**, The spectrum of the terahertz through direct Fourier transform from the terahertz field in **(d)**. **f**, The time-frequency spectrum obtained through wavelet transform from the terahertz field in **(d)**. (All data have been normalized)

Figures S8a and d illustrate the time-domain waveforms of the incident and transmitted THz waves. The frequency domain spectra in Figures S8b and e are obtained through a fast Fourier transform (FFT), clearly revealing the frequencies and absorption characteristics of the two modes of the phonon-polaritons. However, the Fourier transform does not reflect the frequency distribution of the THz waves at different times. In contrast, the time-frequency distribution obtained through wavelet transform, shown in Figures S8c and f, provides a clear representation of the frequency distribution at different times. Especially, the time-frequency distribution in Figure S8f allows for the observation of

the phonon mode at 0.95 THz, which is difficult to discern in the frequency spectrum from the Fourier transform in Figure S8e.

Supplementary Note 6: Evolution of phonon-polariton

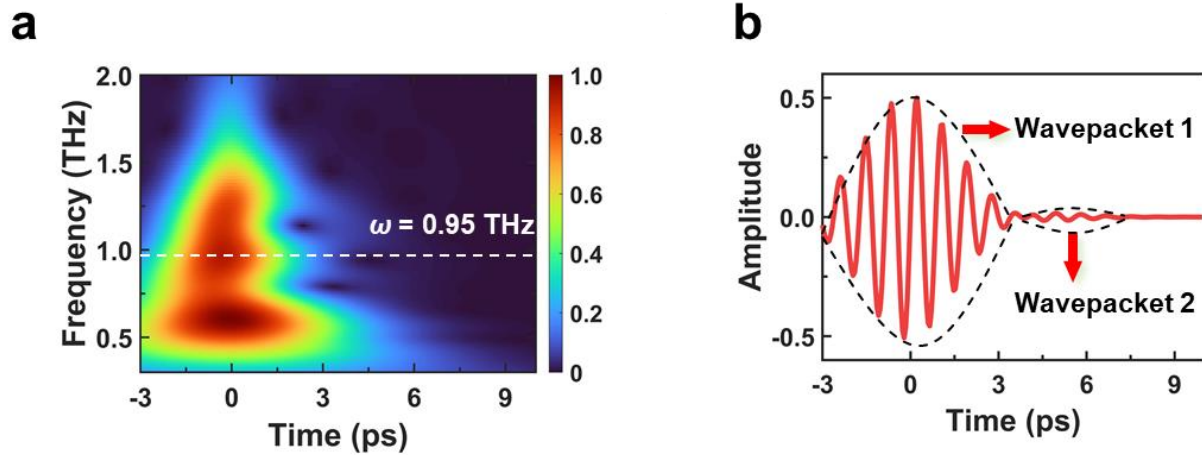


Figure S9 | **a**, The time-frequency domain representation of the terahertz field transmitted through the sample with $d = 4 \mu\text{m}$. The white dashed line indicates the position of the phonon at $\omega = 0.95$ THz. By extracting the terahertz field evolution information along the white dashed line, the mode evolution is presented in **(b)**. **b**, The red curve represents the evolution of the terahertz field at $\omega = 0.95$ THz, while the black dashed lines outline two wavepackets.

Figure S9a displays the time-frequency domain representation for $d = 4 \mu\text{m}$. By extracting the time evolution of the amplitude information at $\omega = 0.95$ THz, we obtain the wavepackets shown in Figure S9b. In wavepacket 1, the terahertz field does not interact with the material, while in wavepacket 2, the terahertz field is associated with phonon re-emission predominates. The amplitude of the wavepacket 2 characterizes the intensity of phonon radiation. By extracting the amplitude of the electric field, we can obtain the intensity and phase variations of the terahertz field at $\omega = 0.95$ THz shown in Figure 5 in the main text. The timing of the intensity and phase discontinuities coincide with the timing of the phonon wavepacket alternation, illustrating the process of phonon absorption and re-emission of terahertz radiation. Using the same method, the electric field evolution at the upper and lower branches of the phonon-polaritons can also be extracted in Figure S10.

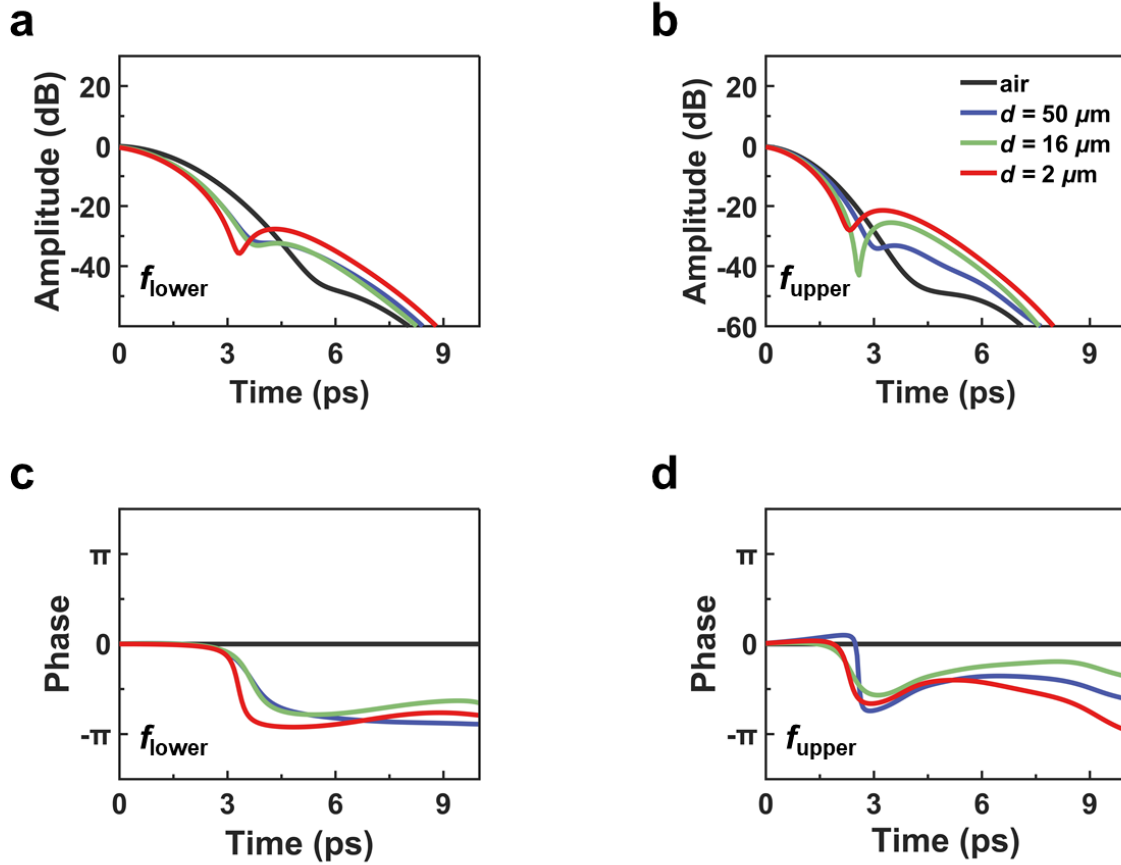


Figure S10 | Time evolution of the intensity and phase of the terahertz field for different parameters d . **a**, The intensity evolution of the lower polariton branch. **b**, The intensity of the upper polariton branch. **c**, The phase evolution of the lower polariton branch. **d**, The phase evolution of the upper polariton branch.

We extracted the upper and lower polariton branches from Figures 4a-d for further analysis of intensity and phase. As shown in Figures S10c-d, a clear phase shift of π is observed, leading to the destructive interference of the far-field radiation at the frequency of upper and lower polariton branches. The nearly simultaneous changes of the intensity and phase with respect to time indicate a strong correlation between the upper and lower polariton branches.

Supplementary Note 7: Sample fabrication

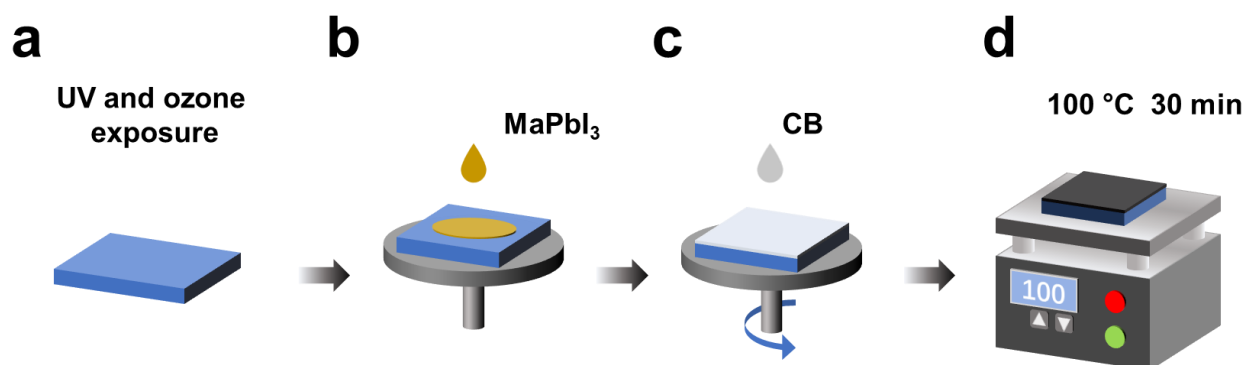


Figure S11 | Preparation steps for perovskite. **a**, The quartz substrate is initially cleaned using UV light and ozone exposure. **b**, After dropping the lead iodide perovskite precursor solution onto the substrate, it is spun at a speed of 6000 rpm to achieve a uniform film of lead iodide perovskite. **c**, During the spin-coating process, toluene solution is added to improve the crystallization of the perovskite film. **d**, After spin-coating, the samples undergo thermal annealing treatment.

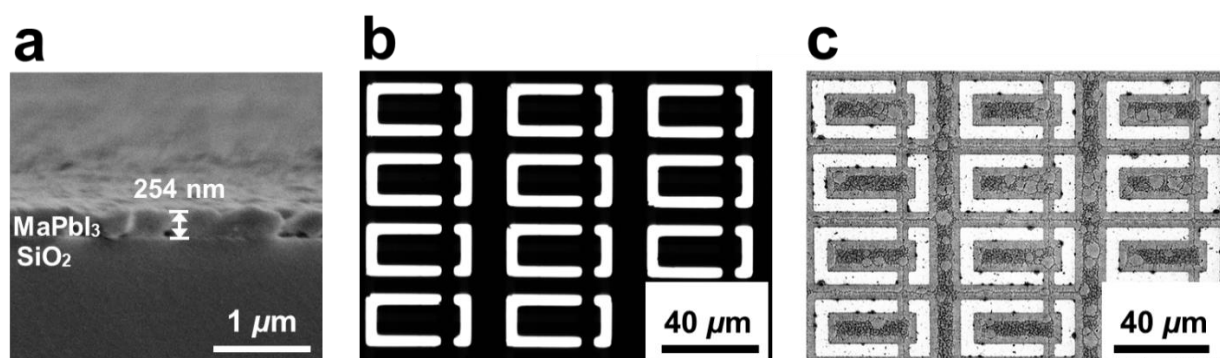


Figure S12 | **a**, MaPbI_3 thin film was spin-coated onto a quartz substrate, and imaged using SEM (Scanning Electron Microscope). **b-c**, Optical images of the metasurfaces; **(b)** before and **(c)** after the spin-coating of MaPbI_3 .

Supplementary Note 8: Experiment setup

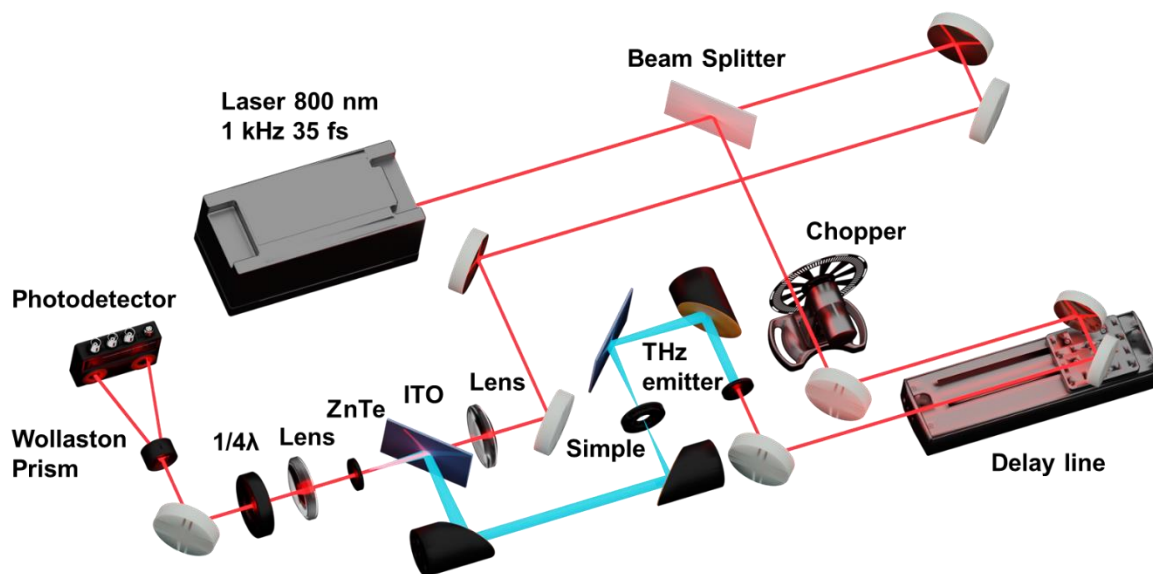


Figure S13 | Schematics of terahertz generation and detection.

The schematic of the experimental setup is shown in Figure S13. The THz-TDS system is driven by a Ti-sapphire femtosecond laser, which generates laser pulses with a duration of 35 fs, a repetition rate of 1 kHz, and a center wavelength of 800 nm. We utilize efficient metallic spintronic emitters of ultra-broadband terahertz radiation to generate terahertz pulses based on the principle of ultrafast photoinduced spin currents. The detection crystal used is ZnTe. To eliminate the influence of water molecules in the air on the experiment, the portion of terahertz propagation is filled with dry air.

Reference

1. Hsu, C. W., Zhen, B., Stone, A. D., Joannopoulos, J. D. & Soljačić, M. Bound states in the continuum. *Nat. Rev. Mater.* **1**, 16048 (2016).
2. Zhao, X. *et al.* Terahertz investigation of bound states in the continuum of metallic metasurfaces. *Optica* **7**, 1548 (2020).
3. Liang, Y., Tsai, D. P. & Kivshar, Y. From Local to Nonlocal High- Q Plasmonic Metasurfaces. *Phys. Rev. Lett.* **133**, 053801 (2024).
4. Koshelev, K., Lepeshov, S., Liu, M., Bogdanov, A. & Kivshar, Y. Asymmetric Metasurfaces with High- Q Resonances Governed by Bound States in the Continuum. *Phys. Rev. Lett.* **121**, 193903 (2018).
5. Sendner, M. *et al.* Optical phonons in methylammonium lead halide perovskites and implications for charge transport. *Mater. Horiz.* **3**, 613–620 (2016).
6. Maggiolini, E. *et al.* Strongly enhanced light–matter coupling of monolayer WS₂ from a bound state in the continuum. *Nat. Mater.* **22**, 964–969 (2023).
7. Wonjoo Suh, Zheng Wang, & Shanhui Fan. Temporal coupled-mode theory and the presence of non-orthogonal modes in lossless multimode cavities. *IEEE J. Quantum Electron.* **40**, 1511–1518 (2004).
8. Fan, S., Suh, W. & Joannopoulos, J. D. Temporal coupled-mode theory for the Fano resonance in optical resonators. *J. Opt. Soc. Am. A* **20**, 569 (2003).
9. Wu, T. & Lalanne, P. Exact Maxwell evolution equation of resonator dynamics: temporal coupled-mode theory revisited. *Opt. Express* **32**, 20904 (2024).
10. Weber, T. *et al.* Intrinsic strong light-matter coupling with self-hybridized bound states in the continuum in van der Waals metasurfaces. *Nat. Mater.* **22**, 970–976 (2023).
11. Zhang, L., Gogna, R., Burg, W., Tutuc, E. & Deng, H. Photonic-crystal exciton-polaritons in monolayer semiconductors. *Nat. Commun.* **9**, 713 (2018).